AN ENHANCED PREDICTION METHODOLOGY FOR RAPID PERFORMANCE AND CONTROL DESIGN OF HIGHLY MANEUVERABLE UAVS

J. Pablo Afman
Research Engineer I

Nicholson Koukpaizan
PhD Candidate

Amanda Grubb
PhD Candidate

Marilyn J. Smith
Professor

School of Aerospace Engineering
Georgia Institute of Technology
Atlanta, Georgia, 30332-0150, USA

ABSTRACT

Unmanned aerial vehicles (UAVs) are capable of rapid, agile maneuvers that were not previously possible in piloted vehicles. Nap-of-the-earth flight in natural and urban terrain, as well as swarm or manned-unmanned teaming flight, requires both accurate quasi-steady aerodynamics and the inclusion of relevant unsteady physics in order to accurately extend current methods for these applications. In this effort, the impact of these aerodynamic assumptions are assessed on vehicle performance and control law design during agile maneuvers. A previously validated reduced-order unsteady aerodynamics model provides an appraisal of the importance of the unsteady terms for UAV flight control, which are shown to result in different trajectories and performance over a maneuver. The sensitivity of the performance and stability of the UAV when simplified canonical configurations are employed is also demonstrated.

NOTATION

c	Reference length (m)
C_F	Force coefficient, $C_F = F/qS$
C_M	Moment coefficient, $C_M = M/qSc$
f	Equivalent frontal cross-section fuselage area (m^2)
F	Force, $\vec{F} = [F_x, F_y, F_z]$ (N)
g	Gravitational constant, $g = 9.81$ (m/s)
I_{ii}	Mass moments of inertia, $I_{ii} = mgd^2T^2/16L\pi^2$ (kg-m^2)
m	Mass (kg)
M	Moment, $\vec{M} = [M_x, M_y, M_z]$ (N-m)
p, q, r	Pitch, roll, and yaw rates (rad/sec)
q_∞	Dynamic pressure, $q_\infty = 0.5\rho V_\infty^2$ (N/m^2)
R_e	Reynolds number, $R_e = \rho V c/\mu$
S	Reference area (m^2)
t	Time (s)
T	Thrust (N)
V	Local velocity (m/s)
V_∞	Freestream velocity (m/s)
x, y, z	Longitudinal, lateral, and normal axes or lengths (m)
u, v, w	Longitudinal, lateral, and normal velocities (m/s)
α	Angle of attack (rad)
β	Yaw angle(rad)
μ	Viscosity (N-s/m^2)
θ, ϕ, ψ	Pitch, roll and yaw angles (rad)
ρ	Density (kg/m^3)
ω	Rotor angular velocity, individual rotors have a subscript i (m/s)

Presented at the 43rd European Rotorcraft Forum, Milan, Italy, September 12–15, 2017.

1 INTRODUCTION

Unmanned Aerial Vehicles (UAVs) are becoming increasingly important in both civilian enterprises and military operations [1]. Because these vehicles can now be lighter and more compact than their counterparts, they are capable of rapid, aggressive maneuvering not previously possible in human-occupied vehicles [2, 3]. Their adaptability makes them sought after for missions such nap-of-the-earth flight in natural and urban terrain either singly, in swarms, or teamed with piloted vehicles [4].

As new design specifications are formulated to exploit the agility and aggressive maneuvers of which these UAVs are capable, computational design and modeling and simulation capabilities must be augmented to include the new physics that these vehicles will encounter. These physics are not trivial, as they

are associated with the nonlinear unsteady aerodynamics that are present during rapid maneuvers.

A secondary, but no less important issue is the development of autonomous flight vehicles. The vehicles are limited to sensor response time, which, in conjunction with agile maneuvers, may lead to slower or larger than anticipated vehicle response due to the transient aerodynamics. This may be particularly true for nap-of-the-earth scenarios where obstacles must be sensed and avoided at high rates of forward flight speed, and where UAVs may be carrying a package such as a sensor or deliverable load [4].

In particular, control design requires a faithful representation of the time-dependent aerodynamic forces and moments acting on the body over the entire mission, including these maneuvers. These dynamic maneuvers will change the steady performance behavior that is typically assigned to the rotors and fuselage, and additional care must be taken when considering structural load limits and control latency during transients and maneuvers. These new requirements have been recognized (e.g., Refs. 5–8), though the focus remains on the steady or quasi-steady aerodynamics aspect of the problem. Mindful of the increased possibility of exceeding structural load limits during maneuvers, advanced flight control system designs that include load alleviation or flight envelope protection schemes have been introduced. Some have included static wind tunnel or computational data to provide more accurate fuselage airloads [9].

Unsteady consideration of the fuselage (nonrotating portion of the vehicle) aerodynamics has been a long-neglected aspect of control law design for maneuvering flight. As a typical example, Laxman et al. [10] focused on adding multiple unsteady rotor dynamics considerations (e.g., Greenberg theory, inertial loads, inflow and vorticity models) during maneuvers, but relegated all of the vehicle (fuselage) dynamics to a simple frontal flat plate drag approximation, $D = 0.5\rho V^2 f C_d$, which is quasi-steady.

Other studies of unsteady aerodynamic effects, focusing primarily on the rotor, have been conducted for specific configurations, such as a quadrotor, but have been limited to quasi-steady global performance effects such as thrust variation with airspeed [5]. In this effort, researchers also studied the impact of the vortex impingement on the fuselage forces as a function of the quasi-static orientation. Their study on shrouds indirectly indicated the importance of considering unsteady aerodynamics terms, yielding variations in the yaw angles of approximately $\pm$ 5° during yaw tracking.

Simulation codes, such as GenHel® apply system identification techniques to determine corrections with orientation rate change. These models are designed for a specific vehicle, in many instances using flight test data [11]. While this approach has shown good correlation for helicopter handling qualities [12], this approach may be extended to early design of future, highly agile UAVs if the reliance on detailed fuselage configurations can be reduced.

New control law design approaches that can be applied to both piloted and autonomous vehicles have been studied. Ozdemir et al. [6] used GenHel® to design a “fly to optimal” (FTO) controller for a compound rotorcraft. Agile maneuvers could involve control limits and control saturation. Robust and perfect tracking (RPT) control approaches have been recommended for UAVs undergoing complex maneuvers [7, 8]. The RPT technique has the goal of remaining an asymptotically stable closed loop system, even when external disturbances and initial conditions (e.g., an obstacle to avoid) are present. They make an assumption of a linearized aerodynamic model based on their flight speed in hover and near hover conditions [8], although low flight speed does not negate the influence of unsteady aerodynamics [13]. Similarly, Marconi and Niadi [14] and Damien [15] focus specifically on robust control of small scale vehicles, such as UAVs, that provide bounded tracking in the presence of uncertainties such as gusts; a transient fuselage model will be key in these designs.

The fuselage, which may or may not be an aerodynamic body, will likely exhibit characteristics during maneuvers that belong in the category of bluff bodies with massively separated flows and unsteady forces and moments. Additionally, UAVs, such as those that carry a payload externally like proposed commercial delivery drones and UAVs with external sensors, may also represent a two-body dynamics problem that includes a bluff body load. It is important to understand how these unsteady loads influence the flight envelope, as well as vehicle stability and maneuverability.

A physics-based, reduced-order model has been developed that computes, in real or near-real time, accurate unsteady aerodynamic forces and moments of both aerodynamic and bluff bodies undergoing rapid and arbitrary motion. It has been applied successfully to analysis of bluff body aerodynamics-dynamic interactions for slung loads [16,17] and is being adopted or evaluated by the U.S. Army for a number of aspects related to slung load research. This model, known as the Georgia Tech Aerodynamics for Bluff Bodies (GTABB), can be easily incorporated into models for control law design and simulation environments to provide accurate transient effects during agile maneuvers and gusts.

This paper evaluates the effects of configuration fidelity, maneuvers, and transients on the aerodynamic performance and control law design for a quadrotor UAV undergoing maneuvers. The effect of the quasi-steady and unsteady terms for the quadrotor body

(fuselage) are isolated from all other unsteady effects (such as the rotor) to illustrate the importance of these effects. The sensitivity of the control law design to simplified quadrotor representations (rectangular box, classic linear flat plate) are examined to determine the importance of these details.

2 UAV CONFIGURATION

The UAV configuration that was used for this demonstration is based on an extant flight test quadrotor, illustrated in Fig. 1. The total UAV size is 0.494 m $\times$ 0.494 m $\times$ 0.222 m (19.45 in $\times$ 19.45 in $\times$ 8.75 in), with a rectangular centerbody that measures approximately 0.122 m $\times$ 0.122 m $\times$ 0.056 m (4.8 in $\times$ 4.8 in $\times$ 2.2 in).

The propulsion system consists of a Multistar Elite 4006 KV740 multirotor electric motor, with a Hobby King 40 amp electronic speed controller that drives four 3-bladed GWS HD-9050x3 propellers.

A bifilar device, a two-support wire vertical-axis torsional pendulum, was used to estimate the inertia of the quadrotor, where the nonlinear equation was simplified by assuming the vehicle angular motion to be small and by omitting damping. This simplification produces a linear equation that yields the three mass moments of inertia, $I_{ii} = [0.0163, 0.0171, 0.0207]^T$ kg-m^2 and a mass of 1.265 kg.

3 MODEL BASED DESIGN

3.1 Physical modeling

The linear kinematic equations of motion for the vehicle are given by the Newton-Euler equations:

$$\begin{aligned} \dot{u} &= vr - wq - g\sin\theta + \mathrm{F_x/m} \\ \dot{v} &= wp - ur + g\sin\phi\cos\theta + \mathrm{F_y/m} \\ \dot{w} &= uq - vp + g\cos\phi\cos\theta + \mathrm{F_z/m} \end{aligned} \tag{1}$$

Similarly, the vehicle angular kinematic equations of motion are given by the Newton-Euler equations, neglecting the cross products of inertia:

$$\begin{aligned} \dot{p} &= qr(I_{yy} - I_{zz})/I_{xx} + M_x/I_{xx} \\ \dot{q} &= pr(I_{zz} - I_{xx})/I_{yy} + M_y/I_{yy} \\ \dot{r} &= pq(I_{xx} - I_{yy})/I_{zz} + M_z/I_{zz}. \end{aligned} \tag{2}$$

composed of components from the angular velocity vector $\vec{\Omega} = [p, q, r]^T$ and the inertia tensor. The set of forces and moments acting on the system are organized in each axis as

$$\begin{aligned} \vec{F} &= F_{gravity} + F_{propulsion} + F_{aerodynamic} \\ \vec{M} &= M_{drag-torque} + M_{propulsion} + M_{aerodynamic} \end{aligned} \tag{3}$$

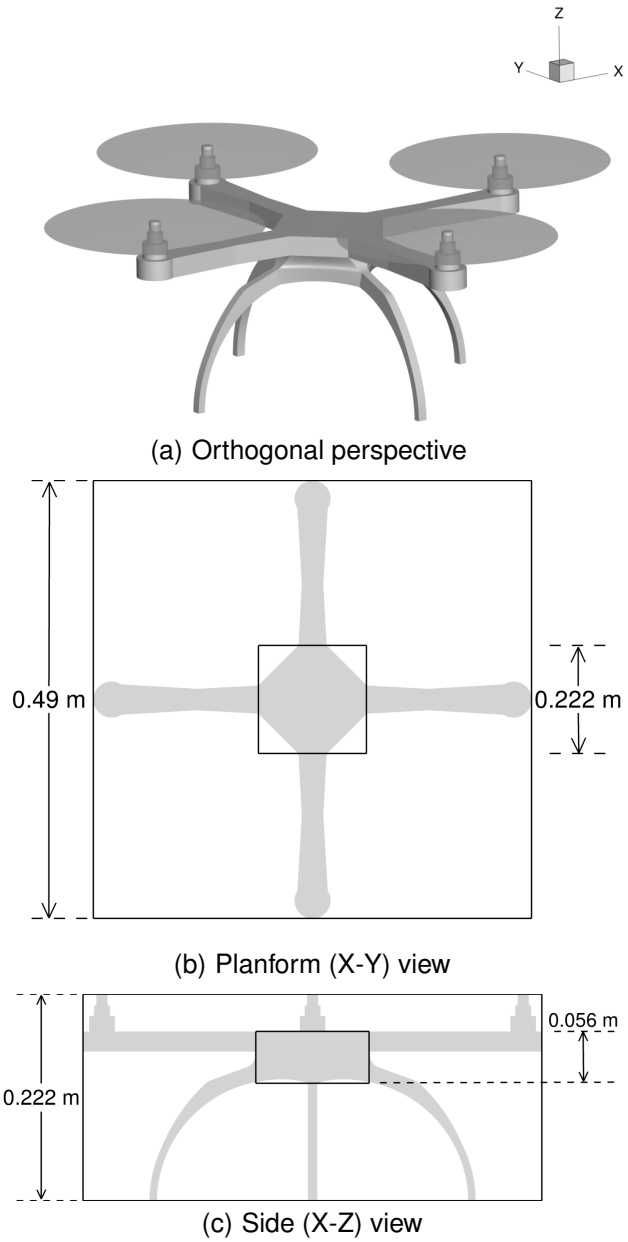

(a) Orthogonal perspective

(b) Planform (X-Y) view

(c) Side (X-Z) view

Fig. 1: Quadrotor UAV configuration.

High fidelity models for $F_{propulsion}$, $M_{propulsion}$, as well as $M_{drag-torque}$, are typically obtained using system identification techniques on real hardware. $F_{aerodynamic}$ and $M_{aerodynamic}$ are often incorporated through simple models based on steady or quasi-steady performance estimations. This work focuses on the implementation and evaluation of unsteady aerodynamic forces and moments necessary for high speed maneuvering.

The rotational kinematic equations were mechanized using quaternions. The inertial velocities are derived from the body-axis velocities by a coordinate transformation (flat-Earth equations are used) and integrated to obtain inertial position. A fourth-order Bogacki-Shampine integration method is applied with a physical timestep of 0.004 seconds.

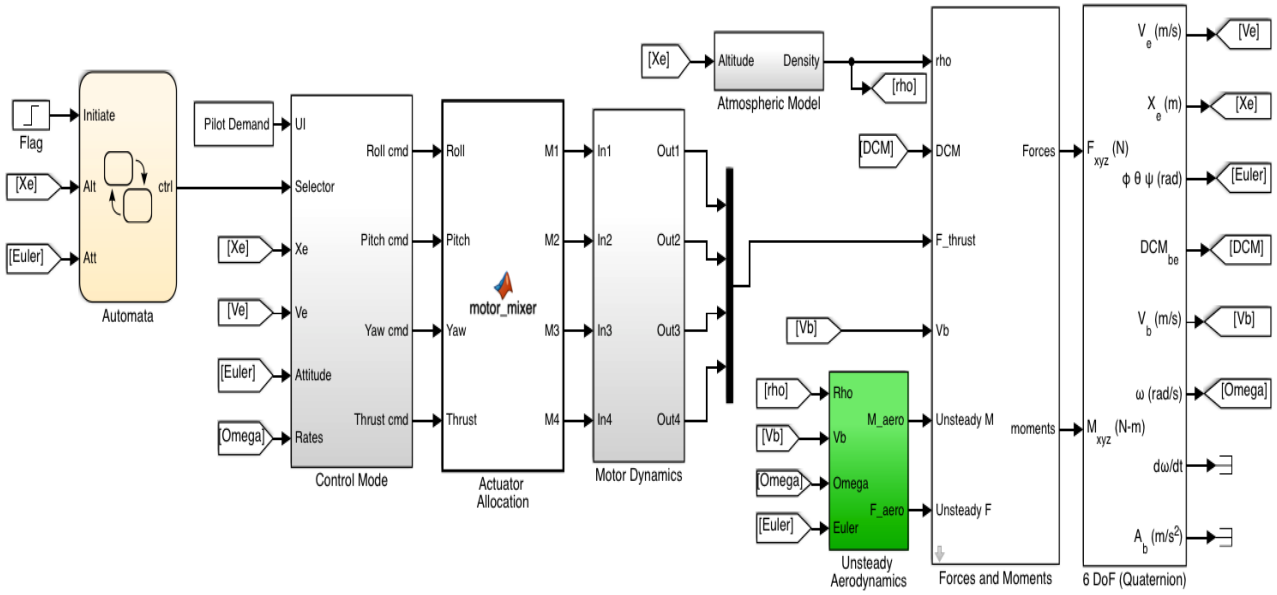

Fig. 2: Model-based design in the Simulink® environment. The unsteady aerodynamics module shown in green.

3.2 Simulation Environment

A simulation environment, such as Simulink®, enables the evaluation of individual model assumptions on the resulting control algorithms, as illustrated by Fig. 2. A direct link can be established between Simulink® and flight simulators, such as FlightGear® to permit visualization.

3.3 System Identification

Control algorithms are developed based on the nominal propulsion plant model. Although design criteria, such as gain and phase margins can ensure acceptable performance in the event of unmodeled or discrepant dynamics, if the dynamics of systems are not captured properly at the design phase, the implementation of the control law into the real system can result in the loss of the vehicle. In order to increase the fidelity of the simulation, system identification was performed on real hardware.

The propulsion identification setup is composed of three load cells, one for obtaining the static thrust curve, and the other two for extracting the drag torque associated with each thrust setting. Furthermore, each load cell is connected to a HX711 24-bit analog-to-digital converter (ADC) amplifier, modified to acquire data at a sample rate of 80 Hz, which enables the accurate acquisition of the transient dynamics. This task enabled understanding of the motor dynamics, as well as the relationship between motor speed and thrust.

The transient dynamics of the motor-propeller combination were obtained using a first order transfer function given by $G_{thrust} = 1/(\tau s + 1)e^{-\gamma s}$ where $\tau = 0.035$ is the identified time constant associated with the transients and $\gamma = 0.09$ is the identified time delay, which is due to the rotational inertia of the rotor. Validation of the propulsion model with experimental data is demonstrated in Fig. 4.

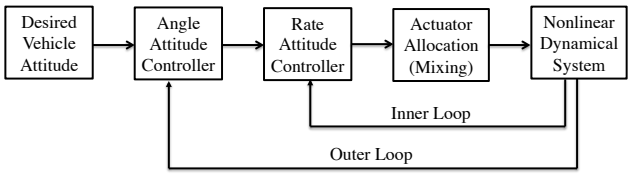

Fig. 3: Nested PID control algorithm.

3.4 Attitude Control

Once the characteristics of the model are known, the derivation of a control algorithm executed by the embedded platform can proceed. The attitude control law employed in the vehicle is the well known cascade feedback controller. After a thorough review of control algorithms for autonomous quadrotors [18], a proportional-integral-derivative (PID) cascade control strategy was chosen due to its simplicity, precision, tracking ability, fast convergence and robustness. Fig. 3 provides a high level overview of this controller. In control theory, the PID controller in a parallel structure is represented in the continuous time domain as:

$$u(t) = K_p e(t) + K_i \int_{t_i}^{t_f} e(\tau)d\tau + K_d \frac{de(t)}{dt}, \quad (4)$$

where K_p, K_i, and K_d represents the proportional, integral and derivative gain components, respectively.

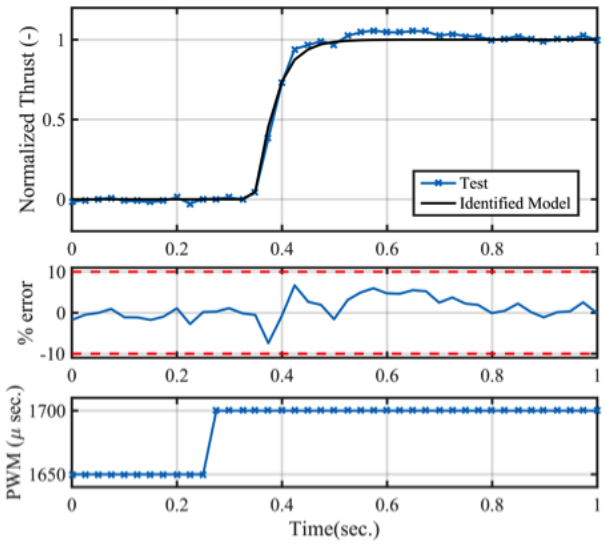

Fig. 4: Validation of control algorithm derived from system identification. PWM is pulse width modulation.

3.5 Actuator Allocation

The actuator allocation block illustrated in Fig. 3 computes the required blade pitch of each variable pitch system in order to generate the appropriate forces and moments required to stabilize and navigate the vehicle. The linear relationship between the forces and moments to the blade pitch of each propeller is given by:

(5)
$$\begin{bmatrix} T \\ M_x \\ M_y \\ M_z \end{bmatrix} = \begin{bmatrix} K_T & K_T & K_T & K_T \\ -K_T L_Y & -K_T L_Y & K_T L_Y & K_T L_Y \\ K_T L_X & -K_T L_X & -K_T L_X & K_T L_X \\ K_D & -K_D & K_D & -K_D \end{bmatrix} \begin{bmatrix} \omega_1^2 \\ \omega_2^2 \\ \omega_3^2 \\ \omega_4^2 \end{bmatrix},$$

where K_T, K_D, L_X and L_Y are the coefficients that make this linear mapping possible.

The derivation and implementation of an enhanced actuator allocation strategy was performed. This modification allows for maximum total thrust, while ensuring that the attitude controller is capable of operating by sizing the input signals when necessary such that saturation never occurs. This approach is based on the observation that for a variable pitch quadrotor, pitch and the roll are affected by the difference in thrust on the opposite pairs of motors. The proposed actuator allocation algorithm ensures that the commanded roll and pitch are the last to reach saturation. Hence, roll and pitch have the highest priority, followed by thrust, then yaw.

4 UNSTEADY AERODYNAMICS MODEL

A reduced-order aerodynamics model to capture the unsteady forces and moments of bluff and aerodynamically-conforming geometries, such as those found in fuselage and UAV bodies has been developed at Georgia Tech [16, 17, 19–22]. This reduced-order model, entitled Georgia Tech Aerodynamics for Bluff Bodies (GTABB) is based on the principles of classic unsteady aerodynamics theory [13] with additional theoretical considerations related to wake shedding associated with finite bluff bodies. Supplementary modules permit the inclusion of unsteady winds and atmospheric turbulence, which have been shown to influence the dynamic airloads for bodies in the quasi-steady and unsteady domains [22]. When applied in the accompanying six-degree-of-freedom simulation code, additional influences such as long tethers and constraints for sling loads and parachutes, are also available [17]. The model is written in both MATLAB® script, providing near real-time ($\sim 1.12t$) results, as well as compiled languages (Fortran, C) that provide faster than real time ($\sim 0.2t$) response. A flowchart describing the GTABB aerodynamics model is provided in Fig. 5. The six-degree-of-freedom capability is described in Refs. 16, 17, 19–22.

The model and its underlying unsteady components (see Fig. 5) have been validated against high fidelity computational fluid dynamics (CFD), wind tunnel tests, and flight tests [16, 17, 19–22]. Figure 6 illustrates the model's ability to capture the nonlinear behavior of a bluff body such as a UAV fuselage. For dynamically varying orientations of the approximately 1:1:1.25 rectangular body, the forces and yaw moments predicted by the GTABB ROM model correlate very well with large eddy simulation-based CFD analyses, even for highly nonlinear behavior [16]. The high frequency behavior observed in the CFD simulations are due to the bluff body vortex shedding. This term is present in the ROM model, but it is omitted for this comparison to improve the clarity of the figures.

Many examples of the GTABB validation with wind tunnel and numerical experiments, as well as flight tests can be found in prior publications [16,17,19–22]. This model is currently under evaluation and further development towards certification by the U.S. Army for use in slung loads operations, including design and simulation.

5 QUADROTOR UAV ANALYSIS

5.1 UAV Quasi-Steady Data

The first step in applying GTABB is to determine the quasi-steady airloads of the underlying configuration to inform the unsteady model per Fig. 5. The configuration force and moment coefficients are needed to encompass the full 360 degree set of combinatorial orientations. These data can be extracted from numerical simulations, physical tests, or theory. However, the many simulations or tests needed to encom-

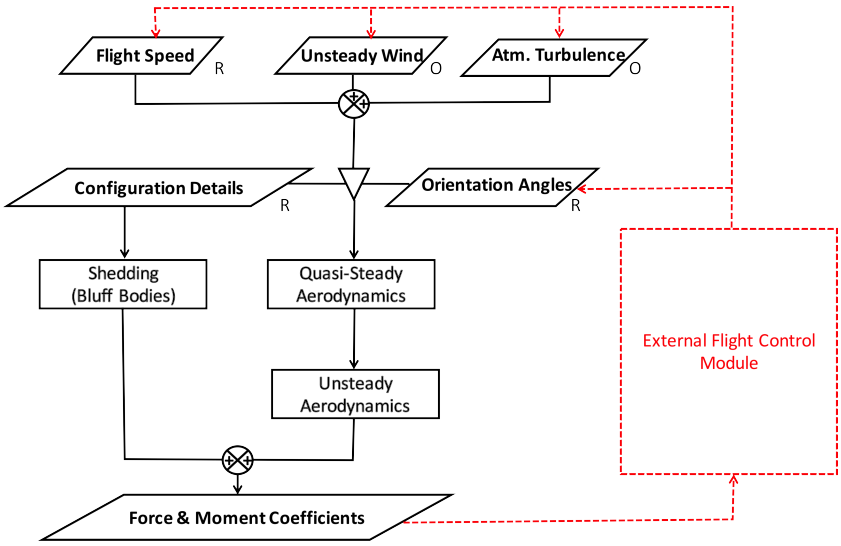

Fig. 5: Algorithm flowchart for the GTABB reduced-order aerodynamic model (solid lines) coupled with a flight system controller (dashed lines), where the data are updated at each time step. Model inputs are marked as optional (O) and required (R).

pass the possible combinations of orientation are cost and schedule prohibitive. Prosser and Smith demonstrated and validated the use of decoupled yaw and angle of attack sweep evaluations which can then be corrected and applied at other combinatorial angles [21]. Further savings in defining the quasi-steady airloads can be implemented by exploiting planes of symmetry.

These data can be obtained from static angles or, employing well-established experimental techniques from the last century, through periodic interrogation of the simulation during quasi-steady rotation (typically at 1–2 rpm). Data are then curve-fitted with a radial basis function and data are extracted at one-degree increments to permit accurate and rapid linear interpolation in the ROM [21].

The quasi-steady data for the centerbody and UAV configuration (Fig. 1) were obtained using a high fidelity unstructured CFD solver, FUN3D [23]. The UAV mesh included a total of 12.7 million nodes, with mixed tetrahedral (background) and prismatic (boundary layer) volume cells. The boundary layer includes 35 normal points for an attached flow with a $y^+ \leq 0.5$ based on a freestream speed of 27 m/s. The control volume outer boundaries extend 20 radii in all directions from the configuration center. The centerbody mesh was generated similarly, but its simpler geometry resulted in an approximate 4 million point mesh. These meshes are based on the recommendations of the grid study conducted by Prosser and Smith [24], which was demonstrated to provide accurate predictions, comparable to physical experiments.

Aerodynamic data were obtained at 5–20 degree increments over an angle of attack range of $\pm 90^\circ$ and a yaw range of 0°–90°, taking advantage of the planes of symmetry. Simulations consisted of steady iterations, followed by additional time-accurate time steps (100 time steps per vortex shedding cycle) for some angles using a hybrid Reynolds-averaged Navier-Stokes/large eddy simulation (HRLES) approach to ensure that the mean aerodynamic performance coefficients were accurately captured [25]. If present, the last two periods of oscillating data were extracted and averaged for the use in the ROM model; most variations were within 2% of the final values.

Coefficients were computed using the standard equations of $C_{F_i} = F_i/qS$ and $C_{M_i} = M_i/qSc$ where $i = 1,2,3$ represents $[x,y,z]$. The reference area, S, was selected as the average of the length and width multiplied by the height of the rectangular centerbody of the UAV. The reference length, c, was taken as the average of the length and width of the centerbody. The moment center is defined at the center of the rectangular box enclosing the UAV.

5.2 Influence of Aerodynamic Shapes

The quasi-steady data computed from the numerical simulations of the UAV configuration (Fig. 1) are illustrated for pertinent forces and moments, Fig. 7 and Fig. 8. Prosser and Smith first published results in 2013 that postulated that the global behavior of the dynamic complex body could be predicted with a similar canonical shapes [26] and this was confirmed in subsequent publications [16, 17]. The quasi-steady coefficients for a 1:1:0.46 rectangular body, similar to the rectangular centerbody of the UAV, are compared with the UAV results in Fig. 7 and Fig. 8. To more readily illustrate the impact of the aerodynamic behavior, the coefficients are scaled with the same references values: $S = 0.00068$ m^2, $c = 0.12192$ m.

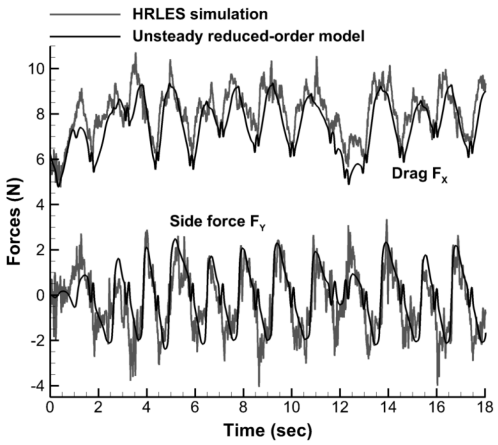

(a) Drag and side forces

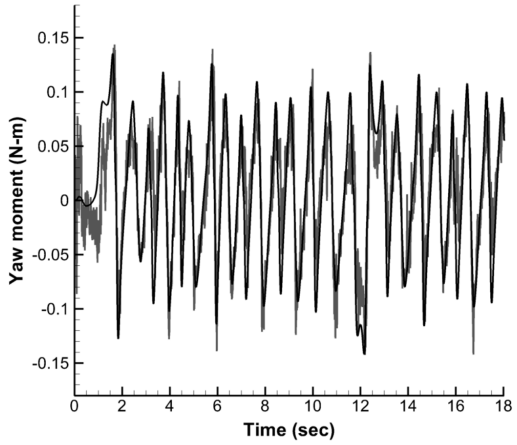

(b) Yaw moments

Fig. 6: Reduced-order model (ROM) and CFD (HRLES) comparison of the dynamic motion of 1:1:1.25 rectangular body suspended from a frictionless gimbal at 40 mph. For legibility, the ROM shedding terms (see Fig. 5) that generate the high frequency oscillations are omitted. Ref. [16]

Included in the these plots are the steady estimates of an equivalent flat plate. In the flat plate model, the aerodynamic moments are zero, and forces in the body frame are given by:

$$F_{\xi_i} = \frac{1}{2}\rho V_{\xi_i}^2 S_{\xi_i} C_{Df} sign(V_{\xi_i}) \tag{6}$$

where, $\xi_i = x, y, z$ for $i = 1, 2, 3$ respectively. $C_{Df} = 1.18$ is the drag coefficient of a square flat plate (Ref. [27]), V_{ξ_i} are the components of the velocity vector in the body frame, and S_{ξ_i} are the frontal areas in the x, y, and z directions.

Equation 6 can be written in the form of

$$F_{\xi_i} = \frac{1}{2}\rho V^2 S C_{\xi_i} \tag{7}$$

where all orientation-dependent components are wrapped into a single aerodynamics coefficient C_{ξ_i} in order to compare the data to the CFD results.

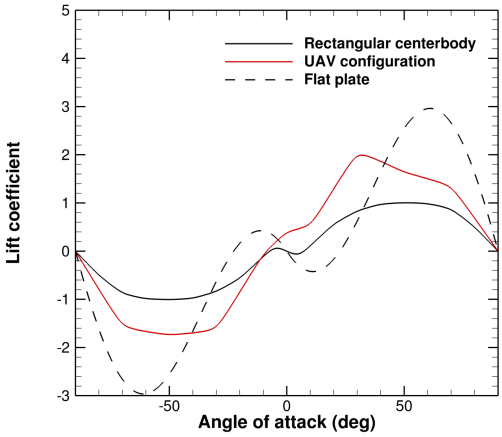

(a) Lift coefficient

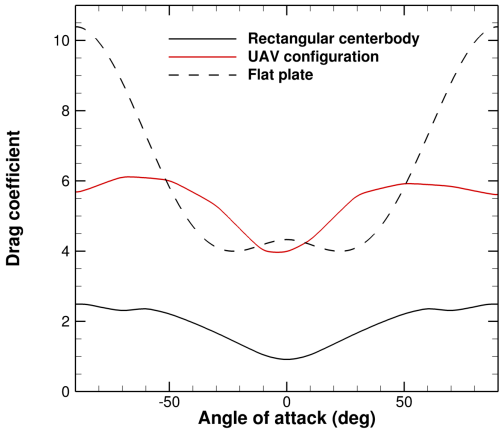

(b) Drag coefficient

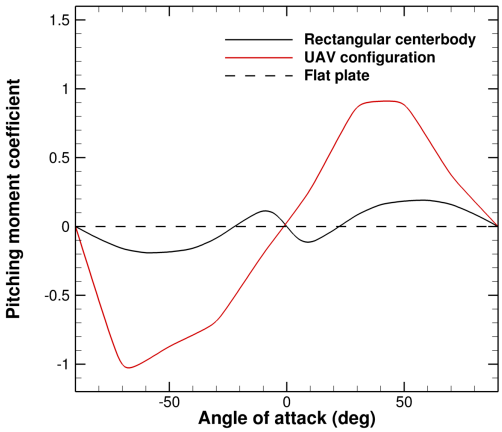

(c) Pitching moment

Fig. 7: Examples of the quasi-steady aerodynamic coefficient data variation over angle of attack.

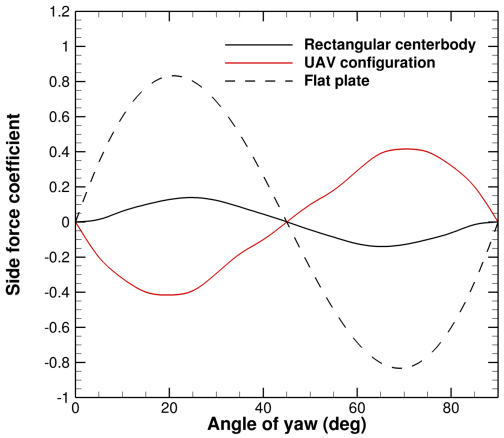

(a) Side force

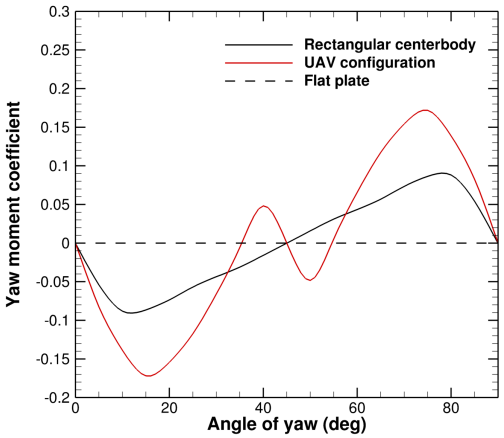

(b) Yaw moment

Fig. 8: Examples of the quasi-steady aerodynamic coefficient data variation over angle of yaw.

For a given pitch or yaw angle, the velocity components in the body frame were computed, followed by the force coefficients in the body frame C_{ξ_i}, which are finally transposed to the wind frame as C_D, C_S, and C_L for comparison purposes.

The overall shape of the aerodynamic coefficients are similar for both bodies, although there are some magnitude and secondary differences. The lift coefficient variation with angle of attack (Fig. 7(a)) provides the most accurate match between the rectangular body and the UAV; the influence of the arms and landing gear of the UAV are primarily observed around the null angle of attack where they act to minimize the abrupt changes in lift due to separation and reattachment. As expected due to the more complex shape of the UAV, the drag is higher than that of the rectangular body (Fig. 7(b)), with similar small differences near the symmetry planes as separation changes dominate. Changes in lift and drag over the yaw angle (β) sweep are minimal and are not shown. The pitching moment (Fig. 7(c)) shows the largest difference, as expected as the box is symmetric, while the UAV has now reversed the orientation of the protuberances, which will impact the moment, leading to only two reversals.

The yaw sweep elucidates some basic differences in the shapes and their corresponding aerodynamic behavior. The moments are again zero based on linear potential aerodynamics theory, where as the centerbody and the UAV both exhibit periodic behavior. The centerbody (rectangular box) and UAV indicate antisymmetric behavior about the 45^o yaw angle, although the UAV has an additional reversal due to the influence of the rotor arms. The side force is particularly interesting as the flat plate estimate will significantly over predict the side force of the rectangular centerbody, but the overall behavior is similar. The UAV, with the addition of the rotor arms and landing gear, actually has a reversal in the force compared to the simplified geometries. This could lead to significant control law errors, as the derivatives will be in the incorrect direction.

The influence of the different configurations on the predicted unsteady aerodynamic behavior is next examined using the GTABB model for the UAV configuration (Fig. 9). The impact of the quasi-steady assumption is first evaluated by examining a step function in angle of attack (Wagner function). The quasi-steady lift follows identically and simultaneously the angle of attack change, while the unsteady behavior shows a lag, as predicted by linear unsteady aerodynamics theory [13]. The vortex shedding terms are not included to improve readability of the figures.

The lift response for the UAV configuration illustrates its similarity to the classic Wagner theory response to an infinite flat plate [13]. A step function of $\alpha = [0^\circ, 5^\circ]$ is applied at $t = 0.5$ s in a freestream of 15 m/s. While the quasi-steady data follow the forcing function, the unsteady data indicate a time lag of approximately 0.5 seconds before reaching its steady state value. Ramping functions illustrate that a one second ramp (5°/sec) results in approximately a 0.25 second delay, but for a three second ramp (1.33°/sec), the aerodynamic response is quasi-steady.

A magnitude increase in the angle of attack forcing function to 25°, well within the nonlinear aerodynamic regime, indicates a change in the lift response curve, though the time lags are approximately the same as the lower angle of attack change. While these changes are small and should not be significant for small or moderate maneuvers, for agile maneuvering where the angular orientations are changing within a second, these small differences have been demonstrated to have a significant effect [16].

A vertical transient climb is modeled in Fig. 10(a). The longitudinal velocity external to the climb maneuver and the climb velocity are both 5 m/s. The indi-

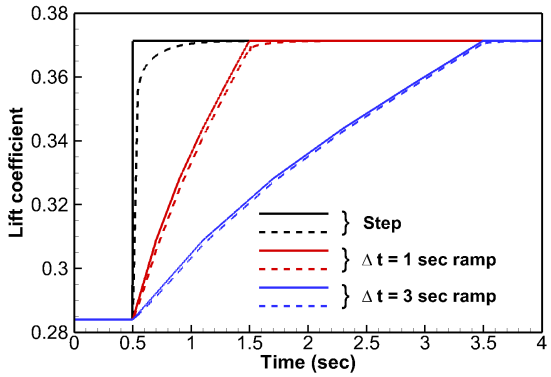

(a) 5° Angle of attack change

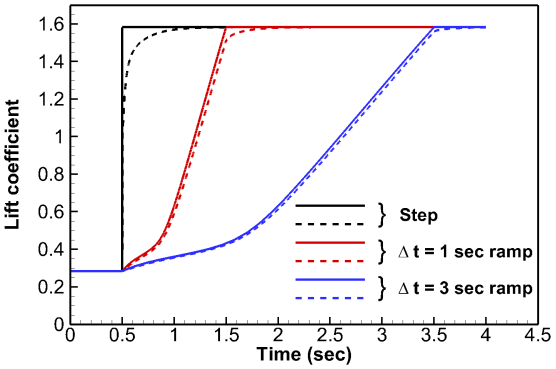

(b) 25° Angle of attack change

Fig. 9: Examples of the quasi-steady and unsteady aerodynamic response to an angular forcing function. Solid lines are quasi-steady results; dashed lines are unsteady results (no shedding).

cial responses for lift (Fig. 10(b)) and drag (Fig. 10(c)) indicate that at the beginning and end of the maneuver, there is a 0.5–1.0 s time lag before the unsteady response reaches steady state. In addition, the impact of the configuration is clear in the rate at which lift changes and the increased drag of the full UAV configuration. Modeling decisions for a rapid translation will impact the thrust requirements at minimum, and potentially actuator limits and structural load limits near margins.

5.3 Autonomous Maneuver

Autonomous aggressive maneuvers enable a broader use of extremely agile vehicles, while reaching the limits of a vehicle's flight envelope. Hence, a control methodology for an autonomous execution of aggressive maneuvers based on human-inspired control logic is employed [2]. The resulting control laws consist of a maneuver execution logic inspired by human pilot strategies, and steady-state trim trajectory controllers, which enable safe recovery from the aggressive transients.

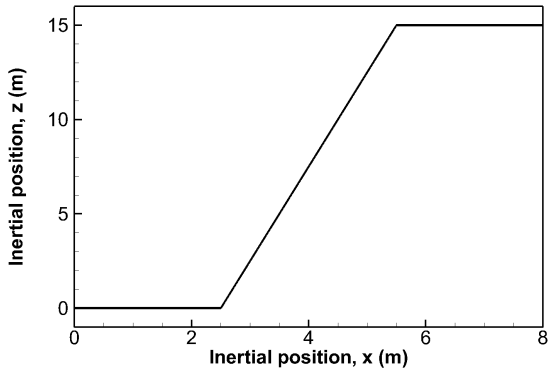

(a) Forcing function

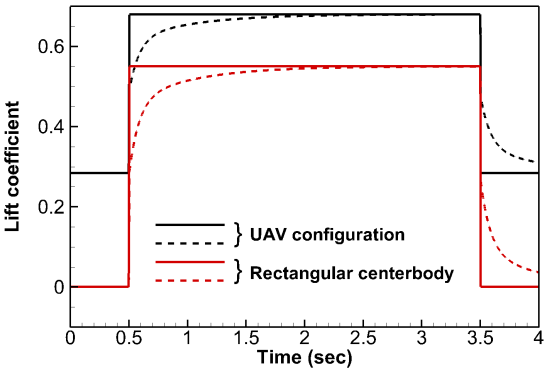

(b) Lift coefficient response

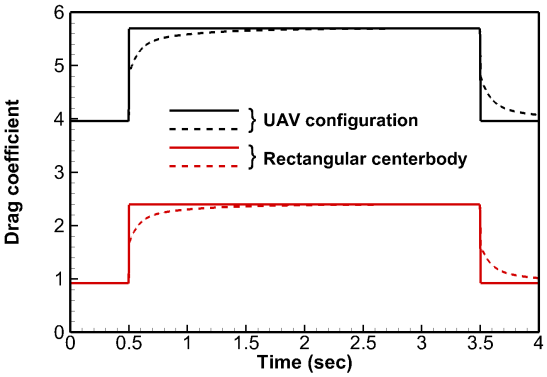

(c) Drag coefficient response

Fig. 10: Unsteady and quasi-steady response to a rapid change in vertical translation. Solid lines are quasi-steady results; dashed lines are unsteady results (no shedding).

While a manual flight mode enables the pilot to fly the auto-stabilized vehicle, where thrust magnitude and attitude angle demands are selected by the pilot, the autonomous maneuver is composed of state transition logic with states in either trim trajectory control modes or maneuver modes. The states are triggered by a predefined set of entry conditions such as altitude, speed, rates, and angles as outlined in Fig. 11.

To demonstrate the differences in the aerodynamics, a split-S maneuver was selected. The split-S con-

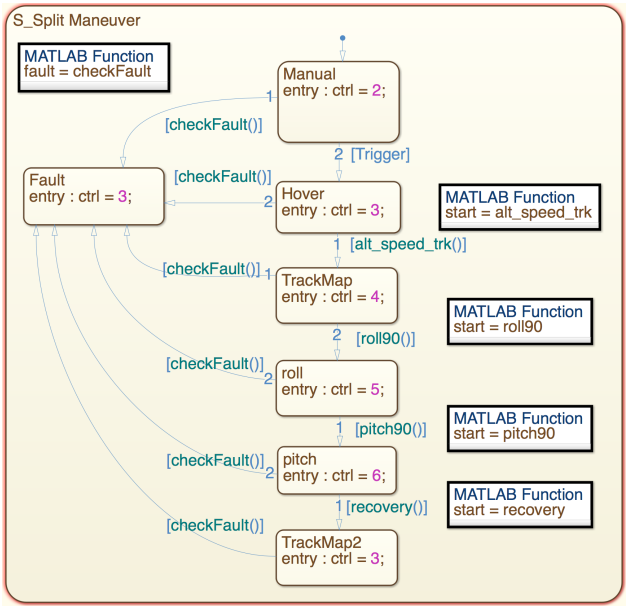

Fig. 11: Autonomous logic represented as state transition logic diagram.

sists of a half-roll inversion followed by a descending half-loop, resulting in flight in the opposite direction at the end of the maneuver. The automated maneuver proceeds as: (1) Vehicle hovers at a specified altitude, and engages the "altitude hold" mode at a safe maneuver altitude; (2) the pilot commands the forward speed setpoint used for the maneuver execution. At this point, the autopilot maintains the altitude and forward speed setpoints. (3) An entirely automatic maneuver sequence is followed, starting with a positive roll of 180°, and rapidly followed by a positive 90° pitch. The vehicle performs the maneuver, and exits the sequence, permitting the trim trajectory control law to recover from the maneuver. (4) At this point the controller automatically returns to the "velocity/heading rate command/altitude hold" mode.

Since the maneuver needs to be executed in a repeatable fashion with guaranteed recovery, individual feedback control laws for maneuver execution and high-bandwidth trim trajectory controllers for smooth recovery were developed. These attitude-stabilizing control laws are illustrated through Fig. 3. During the maneuver, the desired feedback structure was provided by the angular rate tracking controllers, which ultimately bypasses the outer angular loop and executes only the inner rate loop in Fig. 3. Closed loop stability for rate tracking and attitude control loops was obtained by linearizing the model about an expected operating condition, while ensuring adequate phase and gain margins were obtained for each. A similar architecture and approach was used to obtain closed loop stability of the altitude and forward speed control laws. While the altitude control law has the same architecture, where the outputs of the altitude control

Fig. 12: Illustration of simulation environment and vehicle performing Split-S maneuver. Video available at `goo.gl/Gks9nf`.

law become inputs to the altitude rate controller, the forward speed controller augments pitch axis, where outputs of the forward speed controller become the desired pitch attitude. Figure 12 illustrates the simulation environment, where a link to the split-S maneuver has been included.

Since the purpose of this work is to analyze the effects of including complex aerodynamic models in the model based design framework, emphasis is placed on the different transients and trajectories achieved by the vehicle during the maneuver. Figure 13 illustrates the spatial trajectories for the UAV and flat plate aerodynamic models employed in this study.

It is clear in Fig. 13 that the aerodynamic models result in the evolution of three completely different paths with respect to the inertial reference frame. While the flat plate model under approximates the axial drag, resulting in a large deviation along the $Y_{inertial}$ axis, it is also observed to have significant differences in vertical displacement. Vertical displacement during the maneuver is perhaps one of the most important factors, since the vehicle could strike the ground if the maneuver is initialized at a low altitude. Often, designers will predefine a minimum altitude to perform maneuvers while maintaining a safety factor for implementation. If the differences between model and operational scenario are too large, the maneuver could result in loss of the vehicle or payload. Furthermore, the vehicle could be over or under designed in its maneuvering capabilities. Figure 14 illustrates the vertical displacement of the vehicle as a function of time, where different vehicle trajectories can be further discerned.

The trajectory of the rectangular centerbody (Fig. 13) provides similar results to the flat plate during the first part of the maneuver, but the large variation in yaw serves to extend the distance that it takes to complete the maneuver. The quasi-steady and unsteady differences are less pronounced for the centerbody than the UAV, indicating that the UAV arms and landing gear, which are rectangular cross-section

beams, play an important role in the aerodynamic response and should not be neglected. Overall, the rectangular centerbody behaves similarly to the flat plate model, except when the yaw components become very large during the last part of the maneuver. Thus, the remainder of the section will focus on the UAV configuration, with the flat plate as the original aerodynamic baseline.

Figure 13 also serves to illustrate that, while the maneuvering figures that follow (Figs. 14–17) may seem to have small errors between the quasi-steady and unsteady results, these are due to the large scales needed to illustrate the maneuver.

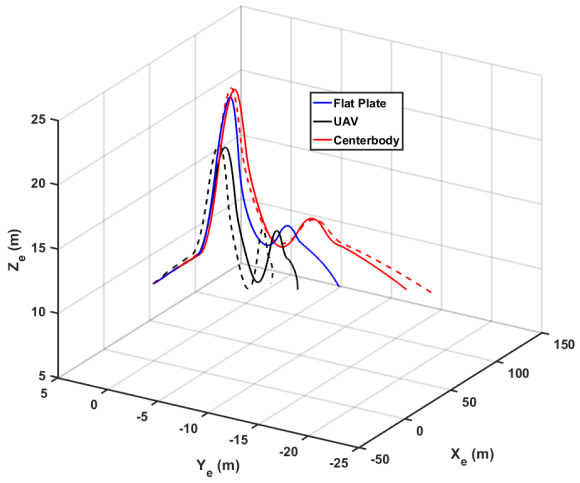

Fig. 13: Trajectory for the UAV and flat plate models in the split-S maneuver. Solid lines indicate quasi-steady results; dashed lines are unsteady results.

The split-S maneuver was designed so that little to no altitude undershoot will occur, permitting the vehicle to perform this evasive maneuver at an altitude of 1m. The altitude in Fig. 14 indicates that performing this maneuver at low altitudes with unsteady aerodynamics effects present will result in the loss of a vehicle at the 1m height. This effect appears to occur due to an under estimation of the vertical drag forces by the flat plate model. This behavior hints that the control designer should include a vertical speed requirement before the autonomous maneuver is initiated.

Figure 14 also shows that the maneuver occurs more rapidly when the unsteady effects are incorporated. This can be observed at the throttle level at approximately 12 to 14 seconds. While the vehicle is inverted, throttle for all rotors is zeroed, and thrust is produced only to maintain the required rates. The unsteady forces and moments (Fig. 15) confirm the under prediction in drag along the vertical vehicle axes through Fz_{aero}. Much more importantly, there exists

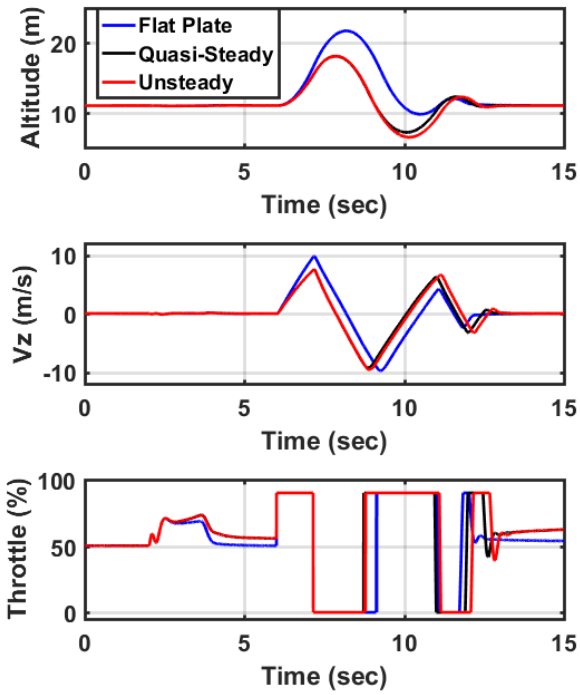

Fig. 14: Split-S maneuver attitude variations for the UAV and flat plate models.

a non restoring moment during the maneuver, which explains why the maneuver states are more rapid for the unsteady aerodynamic case. In the flat plate drag model, all aerodynamic moments are neglected. The introduction of the aerodynamic moments is a then a key driver in the different trajectories observed in Fig. 13 and 14.

Finally, the vehicle attitude and rates (Fig. 17) for the simulated transient contain significant differences between the flat plate drag aerodynamic model and the CFD model. While there appear to be very little differences between the quasi-steady and unsteady aerodynamics due to the plot scaling, the thrust forces produced for each of the rotors reveals significant differences in controller effort required to achieve the maneuver (Fig. 16). This further indicates the importance of unsteady aerodynamic models in model-based design frameworks. Figure 14 illustrates differences in pitch trim angle as the vehicle attempts to track a desired forward velocity. This is a clear indicator of performance under prediction due to simple model effects here, and the potential for similar over- or under-predictions for other maneuvers.

ACKNOWLEDGEMENTS

The investigation was supported by the U.S. Army/Navy/NASA Vertical Lift Research Center of Excellence with Mahendra Bhagwat serving as Pro-

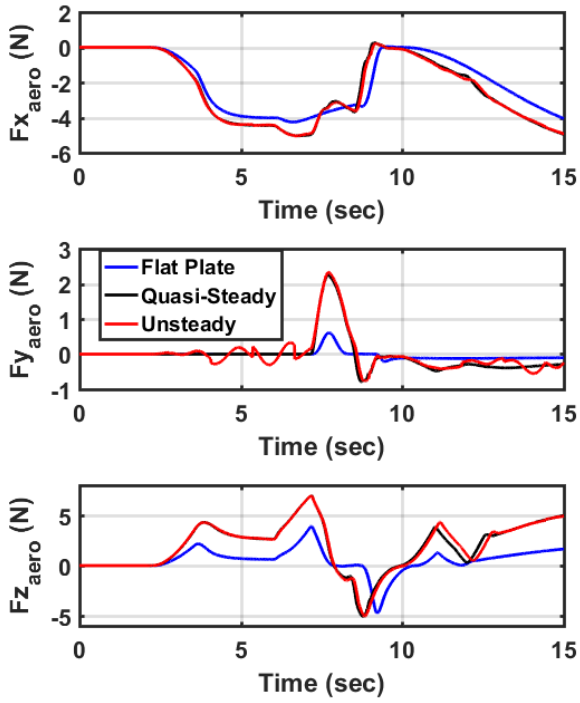

(a) Forces

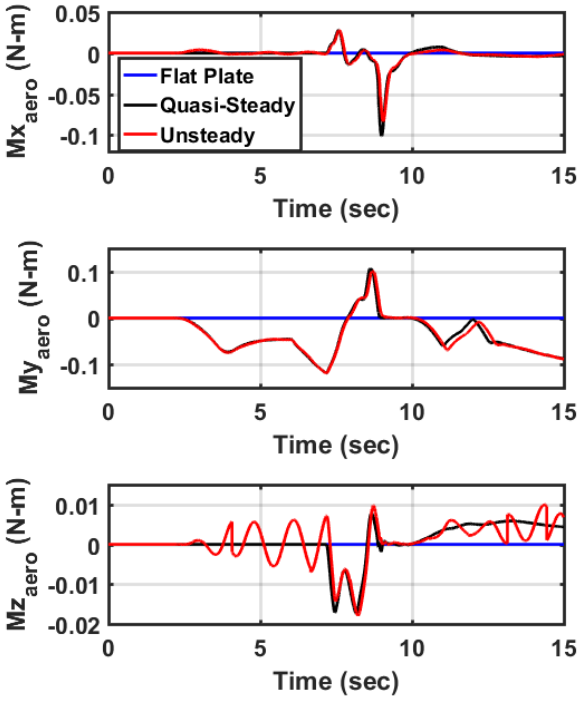

(b) Moments

Fig. 15: Split-S maneuver aerodynamic forces and moments for the UAV and flat plate models.

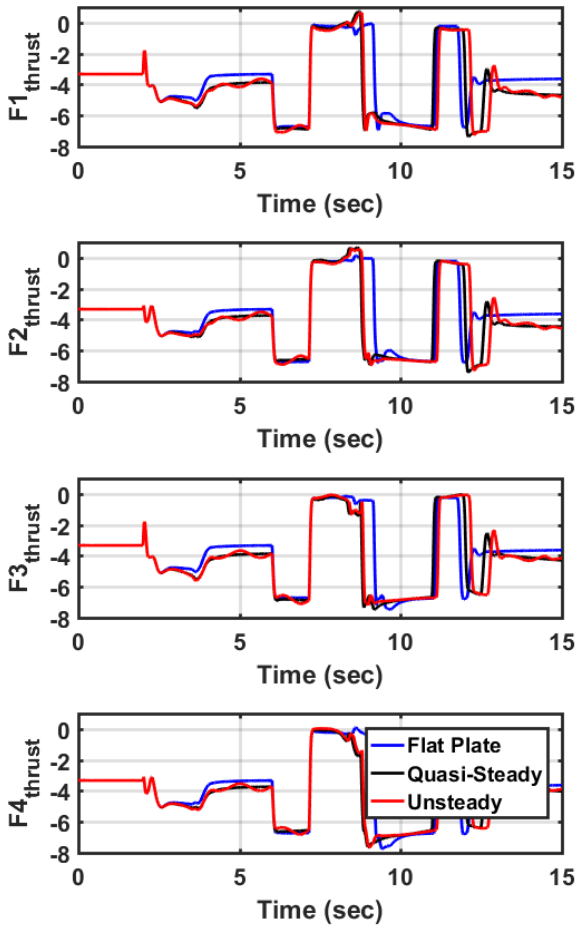

Fig. 16: Thrust differences in the split-S maneuver for the UAV and flat plate models.

gram Manager and Technical Agent, grant number W911W6-11-2-0010.

Computational time was, in part, provided through the Department of Defense (DoD) High Performance Computing Modernization Program (HPCMP) from the DoD HPC Center AFRL DSRC. Roger Strawn was the S/AAA for this time, and his support is gratefully acknowledged.

COPYRIGHT STATEMENT

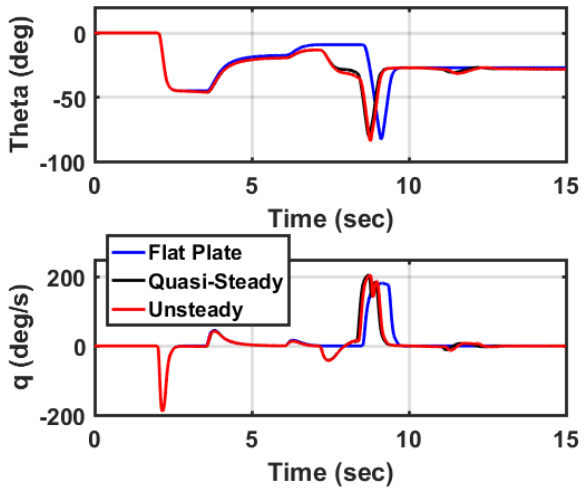

(a) Pitch angle and rate

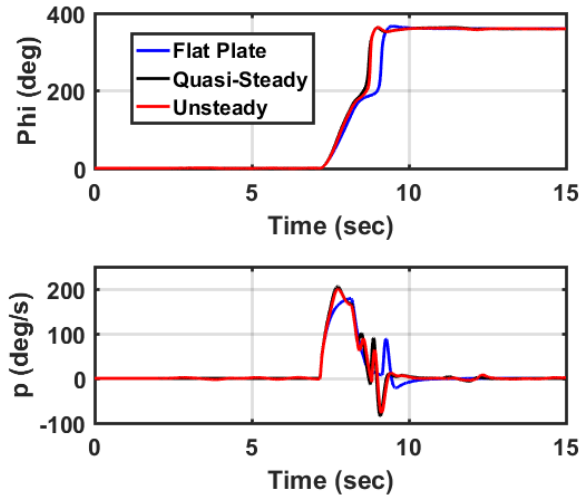

(b) Roll angle and rate

Fig. 17: Split-S maneuver attitude and rates for the UAV and flat plate models.

inal material included in this paper. The authors also confirm that they have obtained permission, from the copyright holder of any third party material included in this paper, to publish it as part of their paper. The authors confirm that they give permission, or have obtained permission from the copyright holder of this paper, for the publication and distribution of this paper as part of the ERF proceedings or as individual offprints from the proceedings and for inclusion in a freely accessible web-based repository.

REFERENCES

[1] U.S. Army UAS Center of Excellence Staff, "U.S. Army Unmanned Aircraft Systems Roadmap 2010-2035," https://fas.org/irp/program/collect/uas-army.pdf, 2010.

[2] Gavrilets, V. and Mettler, B. and Frazzoli, E. and Piedmonte, M. and Feron, E., "Aggressive Maneuvering of Small Autonomous Helicopters: A Human-Centered Approach," *International Journal of Robotics Research*, Vol. 20, (10), 2001, pp. 795–807.

[3] Mettler, B. and Tischler, M. and Kanade, T. and Messner, W., "Attitude Control Optimization for a Small-Scale Unmanned Helicopter," AIAA-2000-4059, AIAA Guidance, Navigation, and Control Conference, Denver, CO, August 2000.

[4] Johnson, E. and Mooney, J., "A Comparison of Automatic Nap-of-the-Earth Guidance Strategies for Helicopters," *Journal of Field Robotics*, Vol. 31, (4), 2014, pp. 637–653.

[5] Hoffmann, G., Huang, H., Waslander, S., and Tomlin, C., "Quadrotor Helicopter Flight Dynamics and Control: Theory and Experiment," Paper AIAA-2007-6461, AIAA Guidance, Navigation and Control Conference and Exhibit, 2007.

[6] Ozdemir, G., Horn, J., and Thorsen, A., "In-Flight Multi-Variable Optimization of Redundant Controls on a Compound Rotorcraft," Paper AIAA-2013-5165, AIAA Guidance, Navigation, and Control (GNC) Conference, 2013.

[7] Cai, G., Wang, B., Chen, B. M., and Lee, T. H., "Design and Implementation of a Flight Control System for an Unmanned Rotorcraft Using RPT Control Approach," Proceedings of the 30th Chinese Control Conference, 2011.

[8] Peng, K., Cai, G., Chen, B. M., Dong, M., Lum, K. Y., and Lee, T. H., "Design and Implementation of an Autonomous Flight Control Law for a UAV Helicopter," *Automatica*, Vol. 45, 2009, pp. 2333–2338.

[9] Voskuijl, M. and Van Tooren, M. J.L. and Walker, D. J. , "Condition-Based Flight Control for Helicopters: An Extension to Condition-Based Maintenance," *Aerospace Science and Technology*, Vol. 42, (4), 2015, pp. 322–333.

[10] Laxman, V., Budiyono, A., Yoon, K. J., and Byun, Y. H., "Improvement of the Parameterized Identification Model Using Quasi-Steady and Nonuniform Inflow Aerodynamic Model," *J. Aerosp. Eng. (USA)*, Vol. 24, (3), 2011, pp. 378 – 88.

[11] Quiding, C., Ivler, C. M., and Tischler, M. B., "GenHel S-76C Model Correlation using Flight Test Identified Models," Proceedings of the American Helicopter Society 64th Annual Forum, Montreal, Canada, April 29 - May 1 2008.

[12] Anonymous, "Aeronautical Design Standard Performance Specification, Handling Qualities

Requirements for Military Rotorcraft, ADS-33E-PRF," https://www.amrdec.army.mil/amrdec/rdmr-se/tdmd/Documents/ads33front.pdf, 2000.

[13] Bisplinghoff, R. L. and Ashley, H. and Halfman, R. L., *Aeroelasticity*, Dover, Mineola, NY, 1983.

[14] Marconi, L. and Naldi, R., "Robust Nonlinear Control of a Miniature Helicopter for Aerobatic Maneuvers," National Aerospace Laboratory NLR - 32nd European Rotorcraft Forum, ERF 2006, Vol. 2, 2007.

[15] Damien, G., *Aerial Vehicles, Unmanned Aerial Vehicle Formation Flight Using Sliding Mode Disturbance Observers*, 2009, Chapter 11, pp. 211 – 234.

[16] Prosser, D. T., *Advanced Computational Techniques for Unsteady Aerodynamic–Dynamic Interactions of Bluff Bodies*, Ph.D. thesis, Georgia Institute of Technology, Atlanta, Georgia, https://smartech.gatech.edu/handle/1853/53899, 2015.

[17] Koukpaizan, N., Movva, J., Butori, M., and Smith, M. J., "Accurate Real-Time Extensible Simulations of Dynamic Bodies," Proceedings of the American Helicopter Society 73rd Annual Forum, May 9-11 2017.

[18] Zulu, A. and John, S., "A Review of Control Algorithms for Autonomous Quadrotors," *Open Journal of Applied Sciences*, Vol. 4, (14), 2014, pp. 547–556.
doi: 10.4236/ojapps.2014.414053

[19] Prosser, D. and Smith, M. J., "Three-Dimensional Bluff Body Aerodynamics and its Importance for Helicopter Sling Loads," Proceedings of the 40th European Rotorcraft Forum, Sept. 2–4 2014.

[20] Prosser, D. and Smith, M. J., "Physics-Based Aerodynamic Simulation Models Suitable for Dynamic Behavior of Complex Bluff Body Configurations," American Helicopter Society 71st Annual Forum, May 2015.

[21] Prosser, D. and Smith, M. J., "A Physics-Based Reduced-Order Aerodynamics Model for Bluff Bodies in Unsteady, Arbitrary Motion," *Journal of the American Helicopter Society*, Vol. 60, (3), 2015, pp. 1–15.
doi: 10.4050/JAHS.60.032012

[22] Nabipour, O., Clinton, J., Ma, T., Prosser, D., and Smith, M. J., "Aerodynamic Influences on the Modeling and Simulation of Instabilities on Dynamic Tethered Loads," Paper AIAA-2016-2141, AIAA Science and Technology Forum and Exposition, January 2016.

[23] Biedron, R. T., Vatsa, V. N., and Atkins, H. L., "Simulation of Unsteady Flows Using an Unstructured Navier-Stokes Solver on Moving and Stationary Grids," Paper AIAA 2005-5093, Proceedings of the 23rd AIAA Applied Aerodynamics Conference, June 6–9 2005.

[24] Prosser, D. and Smith, M. J., "Aerodynamics of Finite Bluff Bodies," *Journal of Fluid Mechanics*, Vol. 799, (6), 2016, pp. 1–16.
doi: 10.1017/jfm.2016.344

[25] Lynch, C. E. and Smith, M. J., "Extension and Exploration of a Hybrid Turbulence Model on Unstructured Grids," *AIAA Journal*, Vol. 49, (11), 2011, pp. 2585–2591.
doi: 10.2514/ 1.56296

[26] Prosser, D. and Smith, M. J., "Navier-Stokes-Based Dynamic Simulations of Sling Loads," Paper AIAA-2013-1922, 54th AIAA/AHS/ASME Structural Dynamics and Materials Conference, April 2013.
doi: 10.2514/6.2013-1922

[27] White, F. M., *Fluid Mechanics*, McGraw-Hill series in mechanical engineering, McGraw Hill, New York, N.Y., 7th edition, 2011.